Article
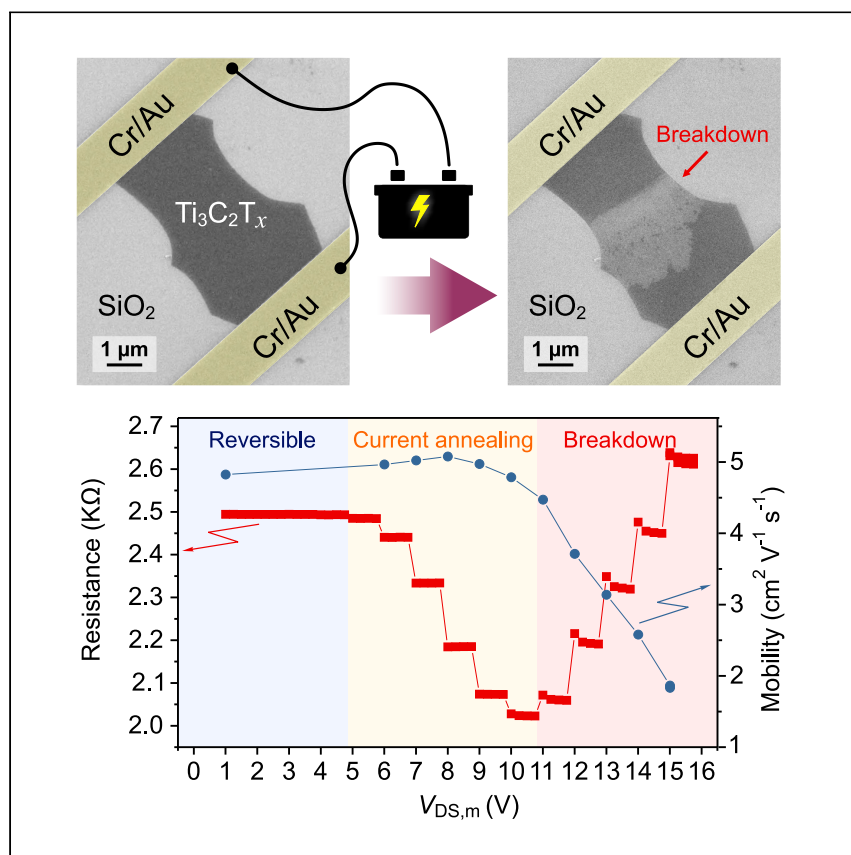
High electrical conductivity and breakdown current density of individual monolayer $Ti_3C_2T_x$ MXene flakes

Alexey Lipatov, Adam Goad, Michael J. Loes, Nataliia S. Vorobeva, Jehad Abourahma, Yury Gogotsi, Alexander Sinitskii

sinitskii@unl.edu

HIGHLIGHTS

Improved electrical conductivity of monolayer $Ti_3C_2T_x$ MXene of up to 11,000 S cm^{-1}

Improved mobility of monolayer $Ti_3C_2T_x$ MXene of up to 6 cm^2 V^{-1} s^{-1}

High breakdown current density of monolayer $Ti_3C_2T_x$ MXene of 1.2 × 10^8 A cm^{-2}

Current annealing of $Ti_3C_2T_x$ devices yields better electronic characteristics

As the scaling down of integrated circuits continues, there is a growing interest in electrically conductive materials with high current-carrying capacity for the next generation of on-chip interconnects. Here, we report that monolayer $Ti_3C_2T_x$ MXene, an emerging two-dimensional material, has a high breakdown current density of 1.2 × 10^8 A cm^{-2}, which exceeds such properties of copper and other conventional metals. The remarkable combination of high electrical conductivity and high current-carrying capacity makes $Ti_3C_2T_x$ promising for interconnect applications.

2 **Benchmark**
First qualification/assessment of material properties and/or performance

Matter

Article

High electrical conductivity and breakdown current density of individual monolayer $Ti_3C_2T_x$ MXene flakes

Alexey Lipatov,[1] Adam Goad,[2,3] Michael J. Loes,[1] Nataliia S. Vorobeva,[1] Jehad Abourahma,[1] Yury Gogotsi,[2,3] and Alexander Sinitskii[1,4,5,*]

SUMMARY

As the scaling down of integrated circuits continues, there is a growing interest in electrically conductive materials with high current-carrying capacity for next-generation on-chip interconnects. Here, we report very high breakdown current density in $Ti_3C_2T_x$ MXene, an emerging two-dimensional material. We performed electrical measurements of individual high-quality monolayer $Ti_3C_2T_x$ flakes, which were prepared by an improved synthesis method, and found that they exhibit electrical conductivities of up to 11,000 S cm^{-1} and field-effect electron mobilities of up to 6 cm^2 V^{-1} s^{-1}, both representing the best values reported for $Ti_3C_2T_x$ flakes so far. All flakes exhibited very similar breakdown current densities of about 1.2×10^8 A cm^{-2}, which are comparable with the best two-dimensional materials, including graphene. The remarkable combination of high electrical conductivity and high current-carrying capacity makes $Ti_3C_2T_x$ promising for nanometer-thin interconnects and warrants investigation of breakdown current densities of other materials from the large MXene family.

INTRODUCTION

Two-dimensional (2D) transition metal carbides, nitrides, and carbonitrides, known as MXenes, are a large family of 2D materials with applications in energy storage, electronics, catalysis, and other fields.[1,2] MXenes have a general formula of $M_{n+1}X_nT_x$, where M is a transition metal, such as Ti, Zr, Nb, V, etc.; X is carbon and/or nitrogen; n = 1, 2, 3, or 4; and T_x represents the surface functional groups.[1-3] Remarkably, while more than 30 different MXenes have been experimentally demonstrated and many others have been predicted theoretically, over 50% of all research efforts so far have been focused on the first discovered MXene, $Ti_3C_2T_x$.[4] The great interest in this material is related to the availability of well-established synthesis procedures,[5] its composition based on earth-abundant elements, as well as extraordinary physical and chemical properties. For example, electrical measurements of individual $Ti_3C_2T_x$ flakes demonstrated their high electrical conductivity of about 4,600 S cm^{-1},[6] while nanoindentation experiments on monolayer $Ti_3C_2T_x$ revealed its effective Young's modulus of 330 GPa, which exceeds the values reported for most other 2D materials.[7]

Interestingly, the combination of high electrical conductivity,[6] which shows only a weak temperature dependence,[8] and stability suggests that $Ti_3C_2T_x$ could possess a high breakdown current density, a technologically important property that has not been discussed with respect to MXenes yet. High current-carrying capacity

Progress and potential

In recent years, the increasing demand for higher performance of integrated circuits has been met by scaling down various device components, including on-chip interconnects. However, as the use of conventional metals, such as copper, in miniaturized interconnects becomes increasingly challenging, there is a growing interest in alternative interconnect materials with high electrical conductivity and breakdown current density. Here, we demonstrate a very high breakdown current density in monolayer $Ti_3C_2T_x$, a material from the family of two-dimensional transition metal carbides known as MXenes, which exceeds such properties of copper and other conventional metals. The remarkable combination of high electrical conductivity and breakdown current density found in $Ti_3C_2T_x$ extends the already impressive list of potential applications of MXenes to microelectronics and warrants investigation of other materials from the large MXene family, some of which may possess even better characteristics.

may extend the already impressive list of potential applications of MXenes to new areas that include high-voltage technologies and on-chip interconnects. As the scaling down of integrated circuits continues, the use of conventional metals, such as copper, in miniaturized interconnects becomes increasingly challenging, because the resistance of metallic wires rises rapidly as their width decreases.[9,10] As a result, there is a growing interest in alternative interconnect materials, and many 2D materials with appreciable electrical conductivities have been tested for interconnect applications. Graphene, the first 2D material that received a wealth of attention from the materials community,[11,12] was shown to exhibit high breakdown current densities on the order of 10^8 A cm^{-2}, which is at least two orders of magnitude larger than that of copper, the most common interconnect material.[13–15] A variety of other 2D materials were also tested for their breakdown current densities, including TiS_3 (1.7 × 10^6 A cm^{-2}),[16] MoS_2 (~5 × 10^7 A cm^{-2}),[17] WTe_2 (~5 × 10^7 A cm^{-2}),[18] $ZrTe_3$ (~10^8 A cm^{-2}),[19] and $TaSe_3$ (~10^8 A cm^{-2}),[20] for some of which the reported values also exceeded such properties of copper and other conventional metals and were comparable with the characteristics of graphene.

Considering the remarkable combination of physical properties of $Ti_3C_2T_x$ and the demonstrated promise of other 2D materials for interconnect applications, in this study, we fabricated field-effect transistor (FET) devices based on monolayer $Ti_3C_2T_x$ flakes and tested their current-carrying capacity to determine how they compare with 2D materials with the highest breakdown current densities reported so far. We utilized $Ti_3C_2T_x$ prepared by the recently reported synthesis method,[21] which yields high-quality monolayer flakes with a Ti:C atomic ratio very close to the ideal value of 1.5 and improved chemical stability. The devices exhibited electrical conductivities of up to 11,000 S cm^{-1} and field-effect electron mobilities of up to 6 cm^2 V^{-1} s^{-1}, both representing an improvement by a factor of two compared with the values reported in our previous study of similar $Ti_3C_2T_x$ FETs.[6] As we increased the drain-source voltages applied to the $Ti_3C_2T_x$ devices, we first observed the improvement in electrical conductivity, which we attribute to the effect of joule heating leading to removal of adsorbed species.[22] This result suggests that current annealing is a useful procedure for improving electrical characteristics of MXene devices. At higher voltages, we observed electrical breakdown of $Ti_3C_2T_x$ devices, which was confirmed by microscopic techniques. All tested devices exhibited very similar breakdown current densities of about 1.2 × 10^8 A cm^{-2}, which are comparable with the best 2D materials, including graphene. The remarkable combination of high electrical conductivity and high current-carrying capacity makes $Ti_3C_2T_x$ promising for interconnect applications and warrants investigation of breakdown current densities of other materials from the large MXene family, some of which may possess even better characteristics.

RESULTS AND DISCUSSION

$Ti_3C_2T_x$ synthesis and characterization

MXenes are synthesized from layered carbides and nitrides with a general formula of $M_{n+1}AX_n$, known as MAX phases,[1,2] and the synthesis protocol plays a crucial role in the functional properties and the environmental stability of the produced material.[6] Reagents used for the MAX phase etching may change the terminal groups (=O, –OH, –F, etc.) in the resulting MXene, altering its electronic properties. Also, harsh reagents can promote the formation of multiple defects in the MXene flakes, which adversely affect their stability in water. Finally, the quality of MXene depends on the crystallinity and grain size of the precursor MAX phase, which are strongly affected by crystal growth conditions. In this work, we synthesized MXene using an improved method presented by Mathis et al.,[21] which produces flakes with significantly better environmental stability compared to the previously reported procedures.[5] This method relies on the use of a precursor

[1]Department of Chemistry, University of Nebraska-Lincoln, Lincoln, NE 68588, USA

[2]A.J. Drexel Nanomaterials Institute, Drexel University, Philadelphia, PA 19104, USA

[3]Department of Materials Science & Engineering, Drexel University, Philadelphia, PA 19104, USA

[4]Nebraska Center for Materials and Nanoscience, University of Nebraska-Lincoln, Lincoln, NE 68588, USA

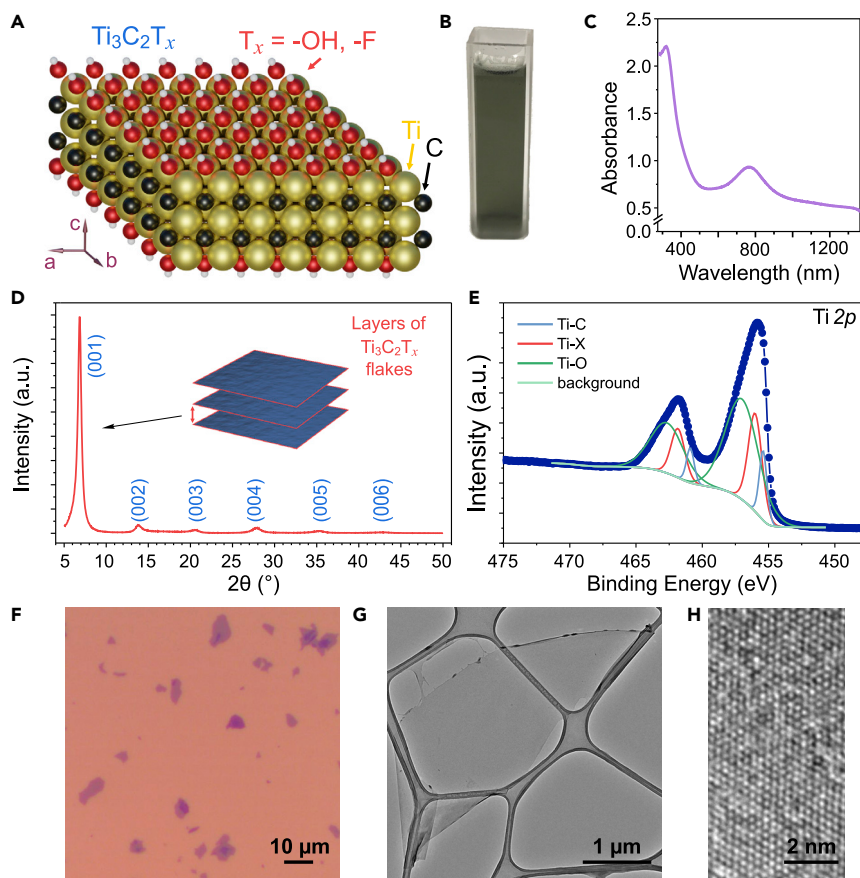[5]Lead contact

*Correspondence: sinitskii@unl.edu

https://doi.org/10.1016/j.matt.2021.01.021

Figure 1. Characterization of Ti₃C₂Tₓ flakes

(A) Scheme of the crystal structure of $Ti_3C_2T_x$ MXene. Yellow spheres, Ti; black spheres, C; the surface functional groups (T_x) are shown as –OH groups (red spheres, O; gray spheres; H).

(B) Photograph of an aqueous colloidal solution of $Ti_3C_2T_x$ in a cuvette.

(C) UV-vis-NIR absorption spectrum of an aqueous colloidal solution of $Ti_3C_2T_x$.

(D) XRD pattern of a $Ti_3C_2T_x$ film.

(E) XPS Ti2p spectrum of $Ti_3C_2T_x$. The dots show the experimental data, while the solid curves show their fitting.

(F) Optical photograph of $Ti_3C_2T_x$ flakes on a Si/SiO₂ substrate.

(G and H) TEM images of an individual monolayer $Ti_3C_2T_x$ flake at different magnifications.

Ti_3AlC_2 MAX phase with improved grain size, stoichiometry, and crystallinity, which was produced using an excess of Al and Ti in the mixture with TiC. After a solid-state synthesis at 1,380°C, the Ti_3AlC_2 particles were washed with HCl and then subjected to selective etching of Al using HF/HCl solution, followed by a delamination to produce large flakes, up to 20 μm in size. It was shown that these $Ti_3C_2T_x$ MXene flakes have a Ti:C atomic ratio very close to the ideal value of 1.5,[21] and a lower concentration of structural defects when compared with the flakes made by other methods.[5] As a result, the $Ti_3C_2T_x$ flakes prepared by this new method had a very long shelf life of several months if stored as aqueous suspensions in ambient conditions, and their oxidation in air started at temperatures 100°C–150°C higher than for similar MXenes produced from a conventional Ti_3AlC_2.[21]

The structure of a $Ti_3C_2T_x$ MXene flake is shown in Figure 1A, demonstrating three layers of Ti in the cubic close packed (ccp) arrangement with carbon atoms occupying the octahedral voids. The $Ti_3C_2T_x$ structure in Figure 1A is oriented in a way

that highlights its relationship with the NaCl-type structure of TiC.[23] While the surface of the $Ti_3C_2T_x$ flake in Figure 1A is schematically shown to be terminated with hydroxyl groups, other terminal moieties, such as =O and –F, were also shown to be present in $Ti_3C_2T_x$ based on the results of X-ray photoelectron spectroscopy (XPS).[24]

The synthesized $Ti_3C_2T_x$ MXene was stored as a colloidal solution in water, which prevented the flakes from aggregating. It was shown that $Ti_3C_2T_x$ flakes synthesized by the improved method can be stored as an aqueous suspension for at least 10 months with only minor degradation of electronic properties.[21] A photograph of an aqueous colloidal solution of $Ti_3C_2T_x$ flakes is presented in Figure 1B. The solution has the green color that is characteristic of $Ti_3C_2T_x$ MXene.[5,25] This color is consistent with the results of optical spectroscopy of an aqueous colloidal solution of $Ti_3C_2T_x$ (Figure 1C), where the minimum absorption in the visible range of spectrum is observed around 520 nm (green). The ultraviolet-visible-near-infrared (UV-vis-NIR) absorption spectrum in Figure 1C is consistent with prior reports for $Ti_3C_2T_x$ MXene.[25]

When a concentrated MXene suspension is dried on a substrate, the flakes are primarily deposited parallel to the surface, forming a layered film that is schematically shown in the inset in Figure 1D. The structure of this layered film can be probed by X-ray diffraction (XRD) analysis, as presented in Figure 1D. The XRD spectrum of a layered $Ti_3C_2T_x$ MXene film in the range of $5° \leq 2\theta \leq 50°$ shows six peaks, which can be indexed as a series of 00l (l = 1, 2, … 6) reflections. Since no other peaks are found in the XRD spectrum, we conclude that the sample does not contain appreciable quantities of crystalline impurities, including the original Ti_3AlC_2 MAX phase. The indexed reflections correspond to the spacing of 1.25 nm, which is larger than the nominal $Ti_3C_2T_x$ monolayer thickness of 0.98 nm.[7] This difference implies the presence of the water molecules trapped between the layers, which is in line with the previously reported data on $Ti_3C_2T_x$ synthesized using the minimally intensive layer delamination (MILD) method.[6]

The results of XPS characterization of drop-casted MXene films were consistent with the previously published data for $Ti_3C_2T_x$.[6,24,26] A high-resolution XPS Ti2p spectrum (Figure 1E) was collected using the pass energy of 20 eV and the step of 0.1 eV. It can be fit with three pairs of components: (1) Ti-C belonging to pure MXene phase (455.4 eV for Ti2$p_{3/2}$ and 460.9 eV for Ti2$p_{1/2}$);[6,24,26] (2) Ti–X from sub-stoichiometric TiC_x (x < 1) or titanium oxycarbides (456.0 eV for Ti2$p_{3/2}$ and 461.9 eV for Ti2$p_{1/2}$);[26] (3) Ti bound to the oxygen surface functional group, which could be represented as Ti_xO_y (457.2 eV for Ti2$p_{3/2}$ and 462.8 eV for Ti2$p_{1/2}$).[26] However, the main result of the XPS characterization is the absence of signals from TiO_2 (458.8 eV for Ti2$p_{3/2}$),[6,24,26] which further confirms the high quality of the studied $Ti_3C_2T_x$ MXene sample.

When a droplet of a diluted $Ti_3C_2T_x$ solution in water was dried on a Si/SiO$_2$ substrate, the size of randomly distributed MXene flakes could be examined by optical microscopy (Figure 1F). Uniformly colored flakes of up to 20 μm in size could be located and later used for device fabrication. Transmission electron microscopy (TEM) imaging allows a more detailed structural characterization of $Ti_3C_2T_x$. Shown in Figure 1G is an individual flake of about 5 μm in size that has a very uniform surface without visible pinholes or foreign particles, which suggests high quality of the MXene material. Partially oxidized $Ti_3C_2T_x$ flakes are known to exhibit pinholes and elongated TiO_2 particles, which tend to predominantly congregate at the

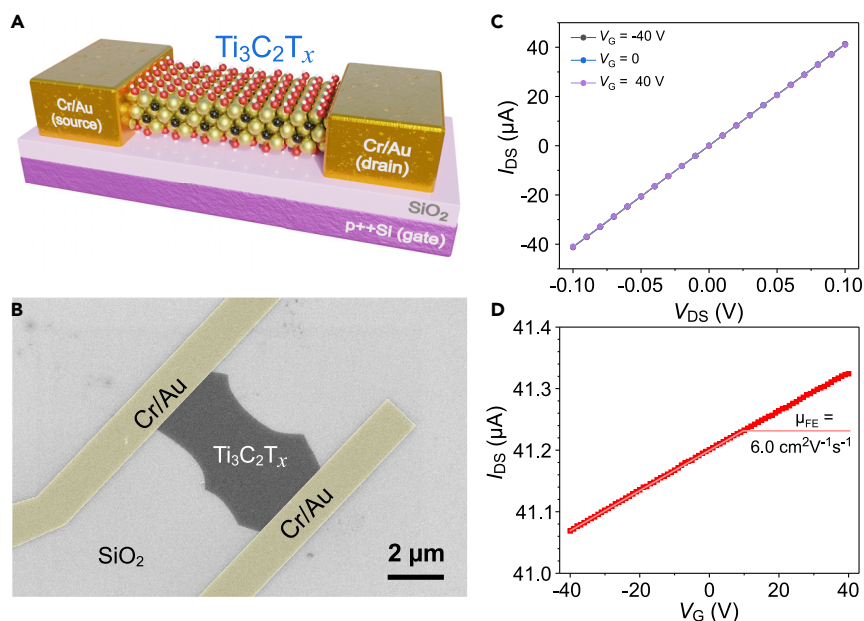**Figure 2. Characterization of electrical properties of Ti$_3$C$_2$T$_x$ flakes**

(A) Scheme of a two-terminal device with a Ti$_3$C$_2$T$_x$ channel.

(B) False-color SEM image of a two-terminal device based on a monolayer Ti$_3$C$_2$T$_x$ MXene flake. The Cr/Au electrodes are colored in yellow for clarity.

(C) I_{DS}-V_{DS} curves obtained from two-terminal measurements of a Ti$_3$C$_2$T$_x$ device shown in (B) at the gate voltages of 40, 0, and −40 V. See also Table S1 for results of the device measurements.

(D) Two-terminal transfer characteristics of a monolayer Ti$_3$C$_2$T$_x$ FET. V_{DS} = 0.1 V.

edges; see examples of TEM images of degraded Ti$_3$C$_2$T$_x$ flakes in Figure S1. High-resolution TEM (Figure 1H) shows the expected hexagonal arrangement of Ti atoms with the average interatomic distance of about 0.302 nm.

Electronic properties of Ti$_3$C$_2$T$_x$ devices

Twelve two-terminal devices with Ti$_3$C$_2$T$_x$ MXene channels were fabricated using the standard electron beam lithography followed by the deposition of 3 nm of Cr and 15 nm of Au. The device scheme is presented in Figure 2A, showing a monolayer Ti$_3$C$_2$T$_x$ flake bridging source (S) and drain (D) electrodes on top of a Si/SiO$_2$ substrate. The heavily p-doped Si substrate served as a bottom gate (G) electrode in the electrical measurements. A scanning electron microscopy (SEM) image of a representative Ti$_3$C$_2$T$_x$ device is shown in Figure 2B; the Cr/Au electrodes are colored in yellow for clarity. The typical channel length in the fabricated devices was about 5 μm. The lateral dimensions of all studied devices are presented in Table S1 for reference.

Electrical characterization of the devices was performed in vacuum at the residual pressure of 2 × 10^{-6} torr after 2 days of evacuation to minimize the effect of surface adsorbates.[27] The I_{DS}-V_{DS} dependencies at three different gate voltages, −40, 0, and 40 V, are shown in Figure 2C. The I_{DS}-V_{DS} dependencies are linear, which is indicative of ohmic contacts between the channel material and the gold electrodes, and nearly coincide, demonstrating a weak modulation of the electrical conductivity of Ti$_3$C$_2$T$_x$ by the gate voltage. The sheet resistances for the devices were calculated from the I_{DS}-V_{DS} curves measured at V_G = 0 and the flake dimensions, see Table S1. The average sheet resistance is 1,160 ± 220 Ω □$^{-1}$. MXene resistivity can be estimated by dividing the sheet resistance by MXene thickness, which, according to

TEM imaging and theoretical calculations, is about 0.98 nm.[28,29] The average resistivity for the nine measured monolayer MXene devices is 1.14 $\pm$ 0.21 $\mu\Omega$ m, with the minimum of about 0.9 $\mu\Omega$ m. These values correspond to the average conductivity of 9,050 $\pm$ 1,620 S cm^{-1} and the maximum conductivity of 11,000 S cm^{-1}, respectively, representing a significant improvement over our previous result of 4,600 S cm^{-1}, which was reported for $Ti_3C_2T_x$ flakes synthesized by the MILD method.[6] Better electronic characteristics could be attributed to the higher quality of $Ti_3C_2T_x$ flakes prepared by the improved synthesis method.[21]

Figure 2D shows transfer characteristics measured in the range of -40 V to $+40$ V applied to the gate electrode. The I_{DS}-V_G dependence is linear and similar to our previous report.[6] The I_{DS} gradually increases when V_G sweeps from negative to positive values, which is indicative of the n-type transport. Field-effect mobilities were extracted from the transfer characteristics of all measured devices using the formula $\mu_{FE} = C_d^{-1} \times \partial\rho^{-1}/\partial V_G$, where C_d is the capacitance of a 300-nm-thick SiO_2 dielectric layer and ρ is the resistivity of MXene channel. As presented in Table S1, the mobilities of the studied $Ti_3C_2T_x$ MXene devices ranged from 3.8 to 6 cm^2 V^{-1} s^{-1}, with four devices showing the maximum value of $\mu_{FE} = 6$ cm^2 V^{-1} s^{-1}. The average value $\mu_{FE} = 5.2 \pm 0.9$ cm^2 V^{-1} s^{-1} is two times larger than our previous report of $\mu_{FE} = 2.6$ cm^2 V^{-1} s^{-1} for the $Ti_3C_2T_x$ flakes synthesized by the MILD method,[6] which further demonstrates the high quality of the MXene material prepared by the improved synthesis method.[21]

Current annealing and breakdown of $Ti_3C_2T_x$ devices

In the following experiment, we studied the effect of gradually increased drain-source voltage on the electronic properties of a MXene channel. In each cycle, the current measurements started at $V_{DS} = 0$, then the drain-source voltage was increased up to a maximum $V_{DS,m}$ (forward sweep), and then returned back to $V_{DS} = 0$ (backward sweep). After that, the device resistance was measured at $V_{DS} = 0.1$ V every minute for 3 min to study the relaxation of the device conductivity over time. Finally, transfer characteristics were recorded at different gate voltages to capture the changes in the field-effect mobility of the device. The next cycle started immediately after that with $V_{DS,m}$ increased by 1 V.

Figures 3A–3C demonstrate the I_{DS}-V_{DS} curves of the $Ti_3C_2T_x$ device shown in Figure 2B at $V_{DS,m}$ ranging from 1 V to 16 V. As the $V_{DS,m}$ gradually increased, the I_{DS}-V_{DS} curves varied significantly and could be grouped into three distinct regions. At low $V_{DS,m}$ values from 1 V to 5 V, the I_{DS}-V_{DS} curves are linear with backward sweeps coinciding with forward sweeps (see Figure 3A). This behavior indicates that the channel material remains unchanged and the device can be safely operated withing this range of V_{DS}.

The second region starts at $V_{DS,m} = 6$ V, and differentiates from the previous region by the backward sweep measuring higher currents than the forward sweep, thus showing a hysteretic behavior (see Figure 3B). It is notable that the I_{DS}-V_{DS} curve of the forward sweep coincides with the I_{DS}-V_{DS} curve for the backward sweep from the previous cycle with lower $V_{DS,m}$, which means that the changes in the electronic properties of the device are permanent. Gradual increase in the slope of I_{DS}-V_{DS} curve at higher $V_{DS,m}$ indicates the increase in the channel conductivity, which can be explained by the effect of current annealing observed in transistors made of other 2D materials, such as graphene.[22] Specifically, current annealing is known to improve contact resistance in graphene and MoS_2 devices. Also, the joule heating may result in the removal of possible photoresist residues,[22] adsorbate species such
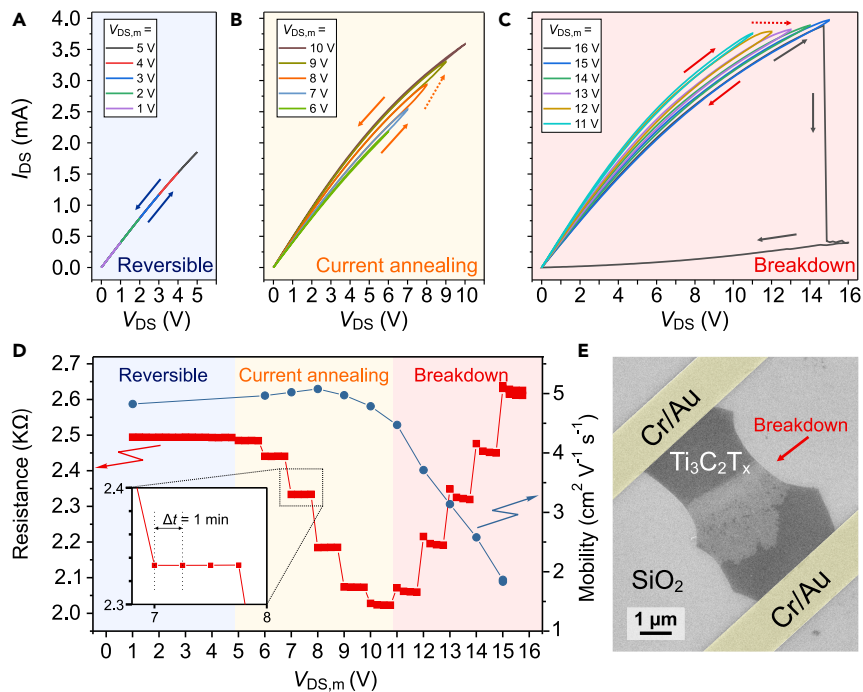
Figure 3. Current annealing and breakdown of a Ti$_3$C$_2$T$_x$ device

(A–C) I_{DS}-V_{DS} curves measured in cycles of gradually increased maximum $V_{DS,m}$ from 1 V to 5 V (A), from 6 V to 10 V (B), and from 11 V to 16 V (C).

(D) Channel resistance (R_{ch}) and field-effect mobility (μ_{FE}) as functions of the maximum drain-source voltage ($V_{DS,m}$) applied to the device. Inset shows that, after each $V_{DS,m}$, four R_{ch} values were measured with 1-min intervals.

(E) False-colored SEM image of the device shown in Figure 2B after its current breakdown at $V_{DS,m}$ = 16 V. See also Figures S2 and S3 for SEM and optical images of other tested devices.

as water molecules,[30,31] as well as some of the functional groups of MXene,[32] further improving transport properties of a channel material.

Finally, the third region starts at $V_{DS,m}$ = 11 V with I_{DS}-V_{DS} curves also showing hysteretic behavior, but with the opposite direction (see Figure 3C). After reaching a certain maximum level (i.e., $I_{DS,max}$ = 3.7 mA for the presented device), the current does not increase with the increase of drain-source voltage, resulting in the I_{DS}-V_{DS} curves at the backward sweeps being lower than the forward sweeps for the same $V_{DS,m}$. The device channel has lower conductance after reaching $I_{DS,max}$ and, since the I_{DS}-V_{DS} curve of the backward sweep coincides with the forward sweep of the next cycle, we conclude that the change is permanent. The hysteresis is observed in the I_{DS}-V_{DS} curves up to $V_{DS,m}$ = 15 V. In the next cycle, shown as a black curve in Figure 3C, the I_{DS} suddenly drops at V_{DS} = 15 V and the backward sweep shows currents significantly lower than recorded in the previous cycles. The change is permanent, and the device shows no I_{DS} dependence on V_G in the transfer characteristics measurements, which can be interpreted as the circuit break due to current breakdown. Indeed, the SEM image shows significant damage to the MXene channel in the central region of the device channel (see Figure 3E).

We studied the dynamics of channel resistance after each cycle for 3 min, as well as the change in the field-effect mobility of Ti$_3$C$_2$T$_x$ MXene. The measurements were performed at V_{DS} = 0.1 V, at a significantly lower bias than the regular sweep measurements with $V_{DS,m}$ ranging from 1 to 16 V. The results of the experiment are shown

in Figure 3D, where the channel resistance (red curve) is measured after each cycle of $V_{DS,m}$ (shown as the horizontal axis) four times with the interval of 1 min. The change in the channel resistance shows similar dynamics with three distinct regions as in Figures 3A–3C . At first, the channel resistance remains the same as before the start of the experiment at R_{ch} = 2.5 KΩ. After the cycle of $V_{DS,m}$ = 6 V, the channel resistance drops by 50 Ω, and remains stable at this level for at least 3 min. In the next cycle at higher $V_{DS,m}$, the channel resistance shows further decline and reaches its minimum of R_{ch} = 2.05 KΩ observed after $V_{DS,m}$ = 10 V. Finally, at higher $V_{DS,m}$ = 11 V and further, the dynamic reverses and the channel resistance starts to increase, showing signs of degradation of the channel material. It is notable that in the last (breakdown) region shown in pink in Figure 3D, after each $V_{DS,m}$ cycle the resistance at V_{DS} = 0.1 V drops slightly after a minute of consecutive measurements. This variation of channel resistance over time was not observed in the previous regions with lower $V_{DS,m}$ and suggests that the device relaxes after considerable joule heating.

The field-effect mobility also undergoes changes after application of high $V_{DS,m}$, but the dynamic is different from the variation of R_{ch} (see the blue curve in Figure 3D). The mobility slightly increases with the increase of $V_{DS,m}$ from its original value of μ_{FE} = 4.8 cm^2 V^{-1} s^{-1} before the experiment and reaches the maximum of μ_{FE} = 5.1 cm^2 V^{-1} s^{-1} after $V_{DS,m}$ = 8 V, after which it starts to decrease and returns back to the original value of μ_{FE} = 4.8 cm^2 V^{-1} s^{-1} after $V_{DS,m}$ = 10 V. It is notable that the peak of mobility occurs in the middle of the current annealing stage, which means that the best device performance is achieved at lower $V_{DS,m}$ than the start of device breakdown. The effect can be explained by degradation of the channel/substrate interface due to elevated temperatures. The decrease of mobility accelerates further at higher $V_{DS,m} \geq$ 11 V, due to the partial breaking of the flake, which effectively reduces the width of the conducting channel. The mobility reaches its lowest value of μ_{FE} = 1.9 cm^2 V^{-1} s^{-1} after $V_{DS,m}$ = 15 V before the complete breakdown.

The maximum current density of monolayer $Ti_3C_2T_x$ was calculated using the equation

$$j_c = \frac{I_{DS,\,max}}{w \cdot t}, \qquad \text{(Equation 1)}$$

where $I_{DS,\,max}$ is the maximum I_{DS} measured before the breakdown, w is the average channel width, and t is the thickness (0.98 nm for the monolayer $Ti_3C_2T_x$).[7,28,29] The data for each measured device are available in Table S2. The maximum current density values for the tested monolayer devices were in the range from 1.04 to 1.44 × 10^8 A cm^{-2}, with the average j_c = 1.21 ± 0.14 × 10^8 A cm^{-2}. The j_c value for $Ti_3C_2T_x$ monolayer is much higher than for 2D materials like MoS_2 and WTe_2,[17,18] and comparable with the materials with the highest j_c values on the order of 10^8 A cm^{-2}: graphene,[13–15] $ZrTe_3$,[19] $TaSe_3$,[20] and metallic single-walled carbon nanotubes.[33] A comparison of maximum j_c values for these and other materials is presented in Table S3.

We investigated the structural damage that occurred to the $Ti_3C_2T_x$ flakes because of the current breakdown by atomic force microscopy (AFM). Figures 4A and 4B show AFM images of the same $Ti_3C_2T_x$ device before and after the experiment; both images were collected at the same conditions. The pristine flake is clean and uniform in thickness but, after the breakdown, the center of the flake is damaged and the area around the break has uneven thickness. Figure 4D shows the height profile of the area with the most significant damage to the device. Upon breakdown, the joule heating produced enough energy to melt the SiO_2 dielectric layer, forming
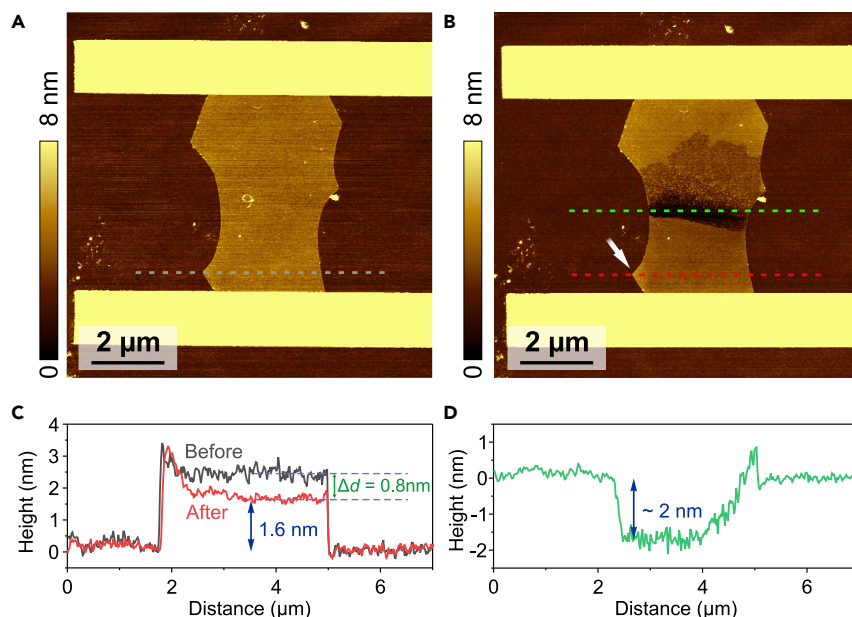
Figure 4. Structural damage of a Ti₃C₂Tₓ flake after the current breakdown

(A and B) AFM images of a $Ti_3C_2T_x$ device (A) before and (B) after the current breakdown. Note that the Cr/Au contacts shown as the horizontal yellow stripes are out of range of the height scale bar.

(C) Comparison of height profiles before and after the breakdown. The corresponding positions are shown in (A) and (B) as gray and red dashed lines.

(D) Height profile of the damaged area of the $Ti_3C_2T_x$ flake measured along the green dashed line in (B).

an indentation of about 2 nm. It should be noted that the melting point of SiO_2 is about 1,700°C, illustrating the enormous current density and the associated joule heating that a monolayer $Ti_3C_2T_x$ can withstand before the breakdown. The flake areas close to the device contacts were unaffected because the Cr/Au leads served as heat sinks. Examples of other $Ti_3C_2T_x$ devices before and after the current breakdown are shown in Figure S2. Previous studies have shown that $Ti_3C_2T_x$ is stable in an oxygen-free environment up to at least 850°C with gradual loss of functional groups upon annealing.[32,34]

Figure 4C shows a comparison of height profiles of the $Ti_3C_2T_x$ flake before and after the current breakdown, which were measured along the same line across the device channel. In its pristine form, the flake thickness is about 2.4 nm, which is similar to the values reported in our previous works for monolayer $Ti_3C_2T_x$ measured on a Si/SiO₂ substrate.[6,35] Interestingly, we previously observed a smaller AFM height of about 1.6 nm for the monolayer $Ti_3C_2T_x$ flakes lying on top of other flakes.[7,35] We suggested that the flakes lying directly on Si/SiO₂ appear thicker in AFM measurements than the flakes lying on other flakes because apparently there is a larger number of adsorbed molecules, such as water, at the $Ti_3C_2T_x$/SiO₂ interface than between the $Ti_3C_2T_x$ layers.[7] Figure 4C shows that, after the current breakdown, the majority of the flake has the thickness reduced by about 0.8 nm down to 1.6 nm. Since the flake has no visible damage in the measured area (Figures 4A–4C), we conclude that the joule heating at high I_{DS} currents resulted in the desorption of the adsorbate molecules trapped between the substrate and the flake, reducing the measured AFM thickness. We observed a similar thickness reduction after annealing $Ti_3C_2T_x$ devices at 300°C in Ar. The change in the thickness of the $Ti_3C_2T_x$ flakes upon current breakdown can also be detected by optical microscopy, as shown in Figure S3.

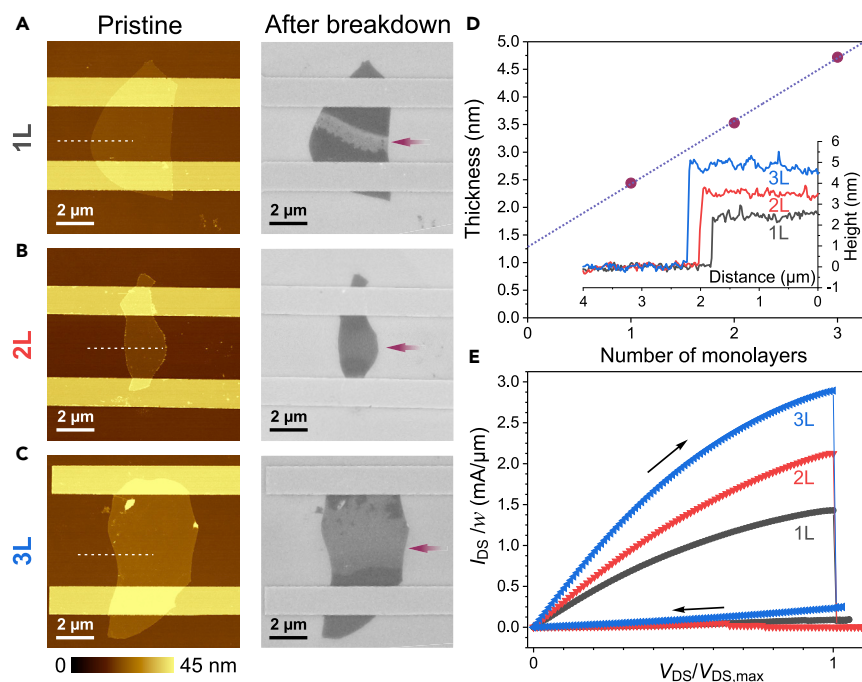**Figure 5. Effect of the Ti₃C₂Tₓ thickness on the current breakdown**

(A–C) AFM and SEM images of devices based on (A) 1L, (B) 2L, and (C) 3L Ti₃C₂Tₓ flakes. AFM images show pristine devices, while SEM images show the same devices after the current breakdown. The height scale bar applies to all AFM images. In SEM images, the damaged areas of the flakes are shown by the purple arrows. See also Figure S3 for optical images.

(D) Dependence of the average AFM thickness of Ti₃C₂Tₓ flakes on the number of monolayers. The dashed line shows the linear fitting of the data. Inset: comparison of the AFM height profiles of the 1L, 2L, and 3L Ti₃C₂Tₓ flakes shown in (A)–(C).

(E) Normalized I_{DS}-V_{DS} curves showing the current breakdown of 1L, 2L, and 3L flakes. The vertical axis is shown as I_{DS}/w, where w is the average width of a Ti₃C₂Tₓ flake. The horizontal axis is shown as $V_{DS}/V_{DS,max}$, where $V_{DS,max}$ is the breakdown voltage for a Ti₃C₂Tₓ device.

It is notable that there is a small protruding region in the bottom left region of the flake, which is indicated by the white arrow in Figure 4B and appears to be unaffected by the electrical measurements, as its thickness does not change upon the current breakdown of the device (Figure 4C). It is likely that, because of the geometry of the flake, this protruding region had a lower current density compared with other regions of the flake along the red line in Figure 4B. However, the fact that this region was not sufficiently annealed by the joule heat generated from other regions of the flake provides an interesting perspective on the likely modest thermal conductivity of Ti₃C₂Tₓ, which is another important property of MXenes requiring further investigation.

While the described synthesis method primarily yields monolayer (1L) Ti₃C₂Tₓ flakes,[21] we occasionally observed bilayer (2L) and trilayer (3L) flakes as well, which were also used for device fabrication and electrical measurements. Figure 5 shows a comparison of the FET devices based on 1L, 2L, and 3L Ti₃C₂Tₓ flakes. Figures 5A–5C demonstrate AFM images of the devices before the electrical measurements, while Figure 5D shows the corresponding height profiles of the 1L, 2L, and 3L Ti₃C₂Tₓ channels of these devices. The thicknesses of the Ti₃C₂Tₓ flakes consistently increase with the number of layers.

SEM images in Figures 5A–5C show the same Ti₃C₂Tₓ FETs after the electrical breakdown. Interestingly, the damaged areas of the device channels, which are

indicated by the purple arrows, could be easily visualized by SEM at the accelerating voltage of 5 kV. The damaged area appears as a relatively narrow strip in the middle of the channel for the 1L $Ti_3C_2T_x$ FET (Figure 5A; also see Figure S2 for SEM images of other devices based on monolayer flakes) but becomes increasingly broad for the 2L (Figure 5B) and 3L (Figure 5C) flakes, suggesting that the joule heating is more delocalized in thicker channels. Despite different thicknesses of the flakes, all devices in Figure 5 exhibited the breakdown current densities comparable with the average $j_c = 1.21 \pm 0.14 \times 10^8$ A cm^{-2} found for monolayer devices: 1.44×10^8 A cm^{-2} (1L; the highest value measured in this work, see Table S2), 1.10×10^8 A cm^{-2} (2L), and 0.98×10^8 A cm^{-2} (3L). In general, the breakdown voltages ($V_{DS,max}$) are expected to be proportional to the channel length (L), while the breakdown currents ($I_{DS,max}$) should be proportional to the channel width (w) and thickness (t).[36] The dependence on the number of layers can therefore be illustrated by plotting the I_{DS}-V_{DS} dependences for the devices shown in Figures 5A–5C in the I_{DS}/w versus $V_{DS}/V_{DS,max}$ coordinates. These dependencies shown in Figure 5E demonstrate that the $I_{DS,max}/w$ values are proportional to the number of layers in the $Ti_3C_2T_x$ flakes in accord with Equation 1. Therefore, while the reported maximum current density of $1.21 \pm 0.14 \times 10^8$ A cm^{-2} was determined from the electrical measurements of $Ti_3C_2T_x$ monolayers, it could be extended to thicker flakes.

Conclusions

In summary, we demonstrated monolayer $Ti_3C_2T_x$ MXene devices with electrical conductivities of up to 11,000 S cm^{-1} and field-effect electron mobilities of up to 6 cm^2 V^{-1} s^{-1}, both representing an improvement by a factor of two compared with the values reported in our previous study of similar $Ti_3C_2T_x$ FETs.[6] We attribute these better characteristics to the higher quality of $Ti_3C_2T_x$ flakes, which were prepared by the improved synthesis method.[21] As we increased the drain-source voltages applied to the $Ti_3C_2T_x$ devices, we first observed the improvement in electrical conductivities and field-effect mobilities, which we explain by the effect of joule heating.[22] At higher voltages, we observed electrical breakdown of $Ti_3C_2T_x$ devices, which was confirmed by microscopic techniques. All tested devices exhibited very similar breakdown current densities of about 1.2×10^8 A cm^{-2}, which are comparable with the best 2D materials, including graphene. The remarkable combination of high electrical conductivity and high current-carrying capacity makes $Ti_3C_2T_x$ promising for interconnect applications and warrants investigation of breakdown current densities of other materials from the large MXene family, some of which may possess even better characteristics.

EXPERIMENTAL PROCEDURES

Resource availability

Lead contact

Further information and requests for materials should be directed to and will be fulfilled by the lead contact, Alexander Sinitskii, sinitskii@unl.edu.

Materials availability

The materials generated in this study are available from the lead contact upon request.

Data and code availability

The data used to support the findings of this study are available from the lead contact upon request.

Materials and reagents

Powders of TiC (99.5%, ∼325 mesh, Alfa Aesar), Ti (99.5%, ∼325 mesh, Alfa Aesar) and Al (99.5%, ∼325 mesh, Alfa Aesar) were used for Ti_3AlC_2 synthesis. HCl (Fisher Scientific), HF (50%, Acros Organics), and LiCl (99.3% Chem-Impex Int.) were used in etching of Ti_3AlC_2 to $Ti_3C_2T_x$ MXene. The produced flakes were deposited on p-type silicon wafers covered with 300 ± 15-nm-thick SiO_2 (Silicon Quest International) for device fabrication.

PMMA950 A4 (4% polymethyl methacrylate in anisole, MicroChem Corp.), methyl isobutyl ketone:isopropanol (1:3) (MIBK:IPA, MicroChem Corp.), isopropanol (IPA, Sigma-Aldrich, 99.5+%), and acetone (Fisher Scientific, 99.7%) were used for electron beam lithography to pattern the electrodes on the $Ti_3C_2T_x$ MXene flakes. Cr (99.995%) and Au (99.999%) targets (International Advanced Materials) were used for electron beam evaporation.

Ti_3AlC_2 synthesis

The MAX and MXene synthesis follow procedures as reported in Mathis et al.[21] A 2:1:1 mass ratio of TiC:Ti:Al powders were mixed by ball mill for 18 h at 70 rpm using a 2:1 mass ratio of zirconia balls to powder. The mixed powder was packed into an alumina crucible, which was then covered with graphite foil and placed into a tube furnace. The tube furnace was purged with argon for 30 min at room temperature. The tube furnace was then heated to 1,380°C for 2 h with a heating and cooling rate of 3°C/min while argon flowed at ∼100 sccm. The sintered Ti_3AlC_2 block was milled into powder with a TiN-coated milling bit. The Ti_3AlC_2 powder was slowly mixed with HCl at a ratio of 10 mL per gram of Ti_3AlC_2 and stirred with a PTFE (polytetrafluoroethylene) magnetic stir bar for 4 h. The Ti_3AlC_2/HCl solution was vacuum filtered using a filter membrane of 5 μm pore size. The filtered Ti_3AlC_2 was washed by repeated filtration of deionized (DI) water through the Ti_3AlC_2 until the filtrate was at pH ∼6. The Ti_3AlC_2 was dried in a vacuum oven for 6 h at 80°C. The Ti_3AlC_2 powder was sieved through a 450-mesh (32 μm) particle sieve and then collected.

$Ti_3C_2T_x$ synthesis

Six milliliters of DI water, 12 mL of 12 M HCl, and 2 mL of 50 wt % HF were added to a 60-mL high-density polyethylene bottle which was left loosely capped throughout to allow gas pressure to escape. One gram of Ti_3AlC_2 was added and mixed with a PTFE magnetic stir bar at 400 rpm for 24 h at 35°C. The multilayer $Ti_3C_2T_x$ was washed with DI water by repeated centrifugation and decantation cycles until the supernatant reached pH ∼6. The solution was centrifuged in a 175-mL centrifuge tube for 5-min cycles at 3,500 rpm, then 0.5 M LiCl solution was prepared by mixing 50 mL of DI water with 1 g of LiCl. The $Ti_3C_2T_x$ was dispersed into the LiCl solution and stirred at 400 rpm for 4 h at room temperature. The $Ti_3C_2T_x$ was then washed with DI water by repeated centrifugation and decantation cycles. Again, the solution was centrifuged in a 175-mL centrifuge tube at 3,500 rpm. For the first wash cycle, the sediment settled after 5 min and the supernatant was decanted. For the four remaining cycles, the sediment settled after 1 h and the supernatant was decanted. Lastly, the $Ti_3C_2T_x$ solution was centrifuged for 15 min and the supernatant was collected.

Device fabrication

PMMA was spin-coated on a Si/SiO_2 substrate with $Ti_3C_2T_x$ flakes at 5,000 rpm for 45 s. Then, the substrate was placed on a hot plate at 180°C for 120 s. A Zeiss Supra 40 field-emission scanning electron microscope and a Raith pattern generator were

used for electron beam lithography to pattern electrodes on $Ti_3C_2T_x$ flakes. After exposure, the substrate was developed in the MIBK:IPA mixture for 60 s, then successively rinsed with 2-propanol and DI water, and dried with nitrogen gas. An AJA electron beam evaporation system at the base pressure of ∼8 × 10^{-9} torr was used to evaporate 3 nm of Cr at 0.1 Å/s rate, which was monitored by a quartz crystal microbalance. This was immediately followed by the evaporation of 15 nm of Au at 0.2 Å/s rate. PMMA and excessive metals were removed by liftoff in hot acetone for 10 min. Finally, the substrate was rinsed with isopropanol and water, and dried with nitrogen gas.

Characterization of $Ti_3C_2T_x$ flakes

SEM was performed using a Zeiss Supra 40 field-emission scanning electron microscope at the accelerating voltage of 5 kV.

TEM of $Ti_3C_2T_x$ flakes was performed using a FEI Tecnai Osiris scanning transmission electron microscope equipped with a high-angle annular dark-field detector and a X-FEG high brightness Schottky field-emission gun. The accelerating voltage was 200 kV.

XPS was performed using a Thermo Scientific K-Alpha X-ray photoelectron spectrometer with a monochromatic Al Kα (1,486.6 eV) X-ray source.

UV-vis-NIR absorption spectra were recorded using a Jasco V-670 spectrophotometer.

XRD patterns were recorded using a Rigaku Smart Lab powder diffractometer with Ni-filtered Cu Kα radiation operated at 40 kV and 15 mA. The 0.03° step and 0.5-s dwelling time were used to collect the XRD patterns.

AFM of $Ti_3C_2T_x$ devices was performed using a Bruker Dimension Icon atomic force microscope operated in PeakForce Tapping mode.

The $Ti_3C_2T_x$ devices were measured in a Lake Shore TTPX cryogenic probe station at a base pressure of about 2 × 10^{-6} torr. The electrical measurements were performed using an Agilent 4155C semiconductor parameter analyzer that was linked to a computer through 82357B USB/GPIB interface and controlled using a National Instruments LabView code.

SUPPLEMENTAL INFORMATION

Supplemental information can be found online at https://doi.org/10.1016/j.matt. 2021.01.021.

AUTHOR CONTRIBUTIONS

A.L. and A.S. designed the experiments. A.L. performed device fabrication, electrical measurements, UV-vis-NIR spectroscopy, SEM and TEM imaging, and data analysis. A.G. and Y.G. synthesized $Ti_3C_2T_x$ MXene. M.J.L. performed AFM imaging and analysis. N.S.V. performed XPS measurements and analysis. J.A. performed powder X-ray measurements and analysis. A.S. and Y.G. supervised the research. A.L. and A.S. wrote the manuscript with contributions from all co-authors. All authors contributed to the discussion and provided feedback on the manuscript.

DECLARATION OF INTERESTS

The authors declare no competing interests.

REFERENCES

1. Gogotsi, Y., and Anasori, B. (2019). The rise of MXenes. ACS Nano 13, 8491–8494.

2. Anasori, B., and Gogotsi, Y. (2019). 2D Metal Carbides and Nitrides (MXenes): Structure, Properties and Applications (Springer International Publishing).

3. Deysher, G., Shuck, C.E., Hantanasirisakul, K., Frey, N.C., Foucher, A.C., Maleski, K., Sarycheva, A., Shenoy, V.B., Stach, E.A., Anasori, B., et al. (2020). Synthesis of Mo_4VAlC_4 MAX phase and two-dimensional Mo_4VC_4 MXene with five atomic layers of transition metals. ACS Nano 14, 204–217.

4. Naguib, M., Kurtoglu, M., Presser, V., Lu, J., Niu, J., Heon, M., Hultman, L., Gogotsi, Y., and Barsoum, M.W. (2011). Two-dimensional nanocrystals produced by exfoliation of Ti_3AlC_2. Adv. Mater. 23, 4248–4253.

5. Alhabeb, M., Maleski, K., Anasori, B., Lelyukh, P., Clark, L., Sin, S., and Gogotsi, Y. (2017). Guidelines for synthesis and processing of two-dimensional titanium carbide ($Ti_3C_2T_x$ MXene). Chem. Mater. 29, 7633–7644.

6. Lipatov, A., Alhabeb, M., Lukatskaya, M.R., Boson, A., Gogotsi, Y., and Sinitskii, A. (2016). Effect of synthesis on quality, electronic properties and environmental stability of individual monolayer Ti_3C_2 MXene flakes. Adv. Electron. Mater. 2, 1600255.

7. Lipatov, A., Lu, H., Alhabeb, M., Anasori, B., Gruverman, A., Gogotsi, Y., and Sinitskii, A. (2018). Elastic properties of 2D $Ti_3C_2T_x$ MXene monolayers and bilayers. Sci. Adv. 4, eaat0491.

8. Miranda, A., Halim, J., Barsoum, M.W., and Lorke, A. (2016). Electronic properties of freestanding $Ti_3C_2T_x$ MXene monolayers. Appl. Phys. Lett. 108, 033102.

9. Steinhögl, W., Schindler, G., Steinlesberger, G., and Engelhardt, M. (2002). Size-dependent resistivity of metallic wires in the mesoscopic range. Phys. Rev. B 66, 075414.

10. Kapur, P., McVittie, J.P., and Saraswat, K.C. (2002). Technology and reliability constrained future copper interconnects. I. Resistance modeling. IEEE Trans. Electron Devices 49, 590–597.

11. Geim, A.K., and Novoselov, K.S. (2007). The rise of graphene. Nat. Mater. 6, 183–191.

12. Novoselov, K.S., Fal'ko, V.I., Colombo, L., Gellert, P.R., Schwab, M.G., and Kim, K. (2012). A roadmap for graphene. Nature 490, 192–200.

13. Murali, R., Yang, Y., Brenner, K., Beck, T., and Meindl, J.D. (2009). Breakdown current density of graphene nanoribbons. Appl. Phys. Lett. 94, 243114.

14. Prins, F., Barreiro, A., Ruitenberg, J.W., Seldenthuis, J.S., Aliaga-Alcalde, N., Vandersypen, L.M.K., and Van Der Zant, H.S.J. (2011). Room-temperature gating of molecular junctions using few-layer graphene nanogap electrodes. Nano Lett. 11, 4607–4611.

15. Yu, J., Liu, G., Sumant, A.V., Goyal, V., and Balandin, A.A. (2012). Graphene-on-diamond devices with increased current-carrying capacity: carbon sp^2-on-sp^3 technology. Nano Lett. 12, 1603–1608.

16. Molina-Mendoza, A.J., Island, J.O., Paz, W.S., Clamagirand, J.M., Ares, J.R., Flores, E., Leardini, F., Sánchez, C., Agraït, N., Rubio-Bollinger, G., et al. (2017). High current density electrical breakdown of TiS_3 nanoribbon-based field-effect transistors. Adv. Funct. Mater. 27, 1605647.

17. Lembke, D., and Kis, A. (2012). Breakdown of high-performance monolayer MoS_2 transistors. ACS Nano 6, 10070–10075.

18. Mleczko, M.J., Xu, R.L., Okabe, K., Kuo, H.-H., Fisher, I.R., Wong, H.S.P., Nishi, Y., and Pop, E. (2016). High current density and low thermal conductivity of atomically thin semimetallic WTe_2. ACS Nano 10, 7507–7514.

19. Geremew, A., Bloodgood, M.A., Aytan, E., Woo, B.W.K., Corber, S.R., Liu, G., Bozhilov, K., Salguero, T.T., Rumyantsev, S., Rao, M.P., et al. (2018). Current carrying capacity of quasi-1D ZrTe$_3$ van der Waals nanoribbons. IEEE Electron Device Lett. 39, 735–738.

20. Empante, T.A., Martinez, A., Wurch, M., Zhu, Y., Geremew, A.K., Yamaguchi, K., Isarraraz, M., Rumyantsev, S., Reed, E.J., Balandin, A.A., et al. (2019). Low resistivity and high breakdown current density of 10 nm diameter van der Waals $TaSe_3$ nanowires by chemical vapor deposition. Nano Lett. 19, 4355–4361.

21. Mathis, T., Maleski, K., Goad, A., Sarycheva, A., Anayee, M., Foucher, A.C., et al. (2020). Modified MAX phase synthesis for environmentally stable and highly conductive Ti_3C_2 MXene. ChemRxiv. https://doi.org/10.26434/chemrxiv.12805280.v1.

22. Moser, J., Barreiro, A., and Bachtold, A. (2007). Current-induced cleaning of graphene. Appl. Phys. Lett. 91, 163513.

23. Lipatov, A., Alhabeb, M., Lu, H., Zhao, S., Loes, M.J., Vorobeva, N.S., Dall'Agnese, Y., Gao, Y., Gruverman, A., Gogotsi, Y., et al. (2020). Electrical and elastic properties of individual single-layer $Nb_4C_3T_x$ MXene flakes. Adv. Electron. Mater. 6, 1901382.

24. Halim, J., Cook, K.M., Naguib, M., Eklund, P., Gogotsi, Y., Rosen, J., and Barsoum, M.W. (2016). X-ray photoelectron spectroscopy of select multi-layered transition metal carbides (MXenes). Appl. Surf. Sci. 362, 406–417.

25. Hantanasirisakul, K., Alhabeb, M., Lipatov, A., Maleski, K., Anasori, B., Salles, P., Ieosakulrat, C., Pakawatpanurut, P., Sinitskii, A., May, S.J., et al. (2019). Effects of synthesis and processing on optoelectronic properties of titanium carbonitride MXene. Chem. Mater. 31, 2941–2951.

26. Peng, C., Yang, X., Li, Y., Yu, H., Wang, H., and Peng, F. (2016). Hybrids of two-dimensional Ti_3C_2 and TiO_2 exposing {001} facets toward enhanced photocatalytic activity. ACS Appl. Mater. Interfaces 8, 6051–6060.

27. Sinitskii, A., Dimiev, A., Kosynkin, D.V., and Tour, J.M. (2010). Graphene nanoribbon devices produced by oxidative unzipping of carbon nanotubes. ACS Nano 4, 5405–5413.

28. Wang, X., Shen, X., Gao, Y., Wang, Z., Yu, R., and Chen, L. (2015). Atomic-scale recognition of surface structure and intercalation mechanism of Ti_3C_2X. J. Am. Chem. Soc. *137*, 2715–2721.

29. Halim, J., Lukatskaya, M.R., Cook, K.M., Lu, J., Smith, C.R., Näslund, L.-Å., May, S.J., Hultman, L., Gogotsi, Y., Eklund, P., et al. (2014). Transparent conductive two-dimensional titanium carbide epitaxial thin films. Chem. Mat. *26*, 2374–2381.

30. Wang, H., Wu, Y., Cong, C., Shang, J., and Yu, T. (2010). Hysteresis of electronic transport in graphene transistors. ACS Nano *4*, 7221–7228.

31. Liu, H., Liu, Y., and Zhu, D. (2011). Chemical doping of graphene. J. Mater. Chem. *21*, 3335–3345.

32. Hart, J.L., Hantanasirisakul, K., Lang, A.C., Anasori, B., Pinto, D., Pivak, Y., Van Omme, J.T., May, S.J., Gogotsi, Y., and Taheri, M.L. (2019). Control of MXenes' electronic properties through termination and intercalation. Nat. Commun. *10*, 522.

33. Javey, A., Qi, P., Wang, Q., and Dai, H. (2004). Ten- to 50-nm-long quasi-ballistic carbon nanotube devices obtained without complex lithography. Proc. Natl. Acad. Sci. U S A *101*, 13408–13410.

34. Seredych, M., Shuck, C.E., Pinto, D., Alhabeb, M., Precetti, E., Deysher, G., Anasori, B., Kurra, N., and Gogotsi, Y. (2019). High-temperature behavior and surface chemistry of carbide MXenes studied by thermal analysis. Chem. Mater. *31*, 3324–3332.

35. Pazniak, H., Plugin, I.A., Loes, M.J., Inerbaev, T.M., Burmistrov, I.N., Gorshenkov, M., Polcak, J., Varezhnikov, A.S., Sommer, M., Kuznetsov, D.V., et al. (2020). Partially oxidized $Ti_3C_2T_x$ MXenes for fast and selective detection of organic vapors at part-per-million concentrations. ACS Appl. Nano Mater. *3*, 3195–3204.

36. Sinitskii, A., and Tour, J.M. (2009). Lithographic graphitic memories. ACS Nano *3*, 2760–2766.